The Astronomical Journal, 126:2662–2676, 2003 December

THE MORPHOLOGICAL DECOMPOSITION OF ABELL 868[1]

S. P. Driver
Research School of Astronomy and Astrophysics, Australian National University, Weston Creek, ACT 2611, Australia; spd@mso.anu.edu.au

S. C. Odewahn, L. Echevarria, S. H. Cohen, and R. A. Windhorst
School of Physics and Astronomy, Arizona State University, Tempe, AZ 85287-1504

S. Phillipps
Department of Physics, University of Bristol, Bristol BS8 1TL, UK

and

W. J. Couch
School of Physics and Astronomy, University of New South Wales, Sydney, NSW 2052, Australia
Received 2003 July 1; accepted 2003 August 29

ABSTRACT

We report on the morphological luminosity functions (LFs) and radial profiles derived for the galaxy population within the rich cluster Abell 868 ($z = 0.153$) based purely on *Hubble Space Telescope* imaging in F606W. We recover Schechter functions ($-24.0 < M_{\rm F606W} - 5\log h_{0.65} < -16.0$) within a $0.65h_{0.65}$ Mpc radius for early (E/S0) , mid (Sabc), and late (Sd/Irr) type galaxies of

1. $M^*_{\rm all} - 5\log h_{0.65} = -22.4^{+0.6}_{-0.6}$, $\alpha_{\rm all} = -1.27^{+0.2}_{-0.2}$;
2. $M^*_{\rm E/S0} - 5\log h_{0.65} = -21.6^{+0.6}_{-0.6}$, $\alpha_{\rm E/S0} = -0.5^{+0.2}_{-0.3}$;
3. $M^*_{\rm Sabc} - 5\log h_{0.65} = -21.3^{+1.0}_{-0.9}$, $\alpha_{\rm Sabc} = -1.2^{+0.2}_{-0.2}$; and
4. $M^*_{\rm Sd/Irr} - 5\log h_{0.65} = -17.4^{+0.7}_{-0.7}$, $\alpha_{\rm Sd/Irr} = -1.4^{+0.6}_{-0.5}$.

The early, mid, and late types are all consistent with the recent field morphological LFs based on recent analysis of the Sloan Digital Sky Survey Early Data Release. From a detailed error analysis, including clustering of the background population, we note that improved statistics can only come from combining data from many clusters. We also examine the luminosity-density and number-density profiles as a function of morphology and draw the following conclusions: (1) the galaxies responsible for the steep faint-end slope are predominantly of late-type morphology; (2) the cluster core is dominated by elliptical galaxies; (3) the core is devoid of late-type systems; (4) the luminosity density as a function of morphological type is skewed toward early types when compared with the field; (5) up to half of the elliptical galaxies may have formed from the spiral population through core disk-destruction process(es). We believe the most plausible explanation is the conventional one that late types are destroyed during transit through the cluster core and that mid types are converted into early types through a similar process, which destroys the outer disk and results in a more tightly bound population of core elliptical galaxies.

Key words: galaxies: clusters: general — galaxies: dwarf — galaxies: evolution — galaxies: formation — galaxies: fundamental parameters — galaxies: luminosity function, mass function

1. INTRODUCTION

The overall luminosity distribution of galaxies in any environment is the traditional tool for describing the galaxy population (see Binggeli, Sandage, & Tammann 1988, hereafter BST88). However, while it categorizes the number density as a function of absolute magnitude, it provides no information on the morphology, structure, spectra, or star formation rates of the contributing galaxies. While studies may show that the luminosity function (LF) of the field, groups and rich clusters are comparable at bright magnitudes (see, for example, De Propris et al. 2003 and Christlein & Zabludoff 2003), this is by no means conclusive proof that the entire galaxy population and characteristics are identical. Indeed, the morphology-density (Dressler 1980; Dressler et al. 1997) and the dwarf population-density (Phillipps et al. 1998) relations clearly tell us that local galaxy density is important and that luminous elliptical galaxies prefer clustered environments, and low-luminosity irregular galaxies field environments. In short, a single luminosity distribution may bypass exactly the information that is required to decipher the subtleties of the environmental dependency of galaxy evolution.

In addition, recent measurements of the LFs in rich clusters have led to inconsistent conclusions as to whether there is a universal LF (see, for example, Trentham 1998) or a dwarf population–density relation (Phillipps et al. 1998). In a study of seven Abell clusters, Driver, Couch, & Phillipps (1998a), using a statistical background subtraction method, found significant variation in the faint-end slopes whereby low-density clusters exhibit steeper slopes (or higher dwarf-to-giant ratios). The same result was independently found

[1] Based on observations made with the NASA/ESA *Hubble Space Telescope*, obtained at the Space Telescope Science Institute, which is operated by the Association of Universities for Research in Astronomy, Inc., under NASA contract NAS 5-26555. These observations are associated with program No. 8203.

for a separate sample of 35 clusters by Lopez-Cruz (1997).[2] However, both methods rely on a statistical subtraction of the background population, which, although rigorously tested in Driver et al. (1998b), has been criticized by Valotto, Moore, & Lambas (2001) as being susceptible to cosmic variance along the line of sight—although, it is difficult to understand how cosmic variance can lead to the relatively clean relation between luminosity and local density seen by Phillipps et al. (1998) and the smooth radial increase in dwarf-to-giant ratios seen in A2554 (Smith, Driver, & Phillipps 1997) and A2218 (Pracy et al. 2003). More recently, Barkhouse & Yee (2002) report a general trend of an increase in faint-end slope with cluster radius from $\alpha = -1.81$ to -2.07 for a sample of 17 nearby clusters. For very local clusters where cluster membership can be ascertained more easily, such as Virgo and Coma, Trentham & Tully (2002) summarize the state-of play and argue for a universal LF (see also review by Driver & De Propris 2003 and references therein). Trentham & Hodgkin (2002), however, argue the opposite noting the significant difference in dwarf-to-giant ratio between Virgo and Ursa Major. Some part of this confusion most likely comes about from the apparent different clustering of the two dwarf populations. For example Sandage, Binggeli, & Tammann (1985) found a generally centrally concentrated distribution of dwarf elliptical galaxies in Virgo, whereas Sabatini et al. (2003) report to the contrary a significant steepening in the luminosity function faint-end slope with clustercentric radius, also in Virgo, due to low surface brightness dwarf irregular galaxies. In the Coma Cluster, Thompson & Gregory (1993) identify three dwarf populations (dI's, dE's, and dSph's) each with distinct clustering signatures.

Taken together, the sparse information contained within a single LF and the contradictions in the literature, it seems necessary to deconstruct the LF further, incorporating morphological/structural and/or color information in the analysis. It is also worth noting that some component of the confusion may arise from radial dependencies and the specific areal extent over which the cluster has been surveyed—particularly if the above radial trends seen in Virgo are confirmed as universal. To this end, we have embarked upon a detailed observational program, including space-based optical and X-ray observations and ground-based narrowband imaging, of the rich cluster A868. In this paper, we focus purely on the morphological aspects based upon a 12 orbit Wide Field Planetary Camera 2 (WFPC2) mosaic of the cluster A868. In particular, we are interested in the suggestion that there may exist a universal LF for each morphological type (BST88) and that only the relative normalization changes with environment. Analysis of the Two-Degree Field Galaxy Redshift Survey by De Propris et al. (2003) find that although the overall luminosity distribution is invariant between the field and cluster composite, differences do arise when subdivided according to *spectral* type. Christlein & Zabludoff (2003) confirm this result based on their independent spectral study of the population in and around six low-redshift clusters. These latter results, based on spectral classifications, generally supports the developing notion that star formation is quenched in the infalling galaxy population (Lewis et al. 2002; Gómez et al. 2003; see also review by Bower & Balogh 2003), unfortunately spectral classifications cannot address whether the population has *physically* changed as well.

The cluster A868 itself, is unremarkable, except that it formed part of a cluster population study by Driver et al. (1998a), in which a high dwarf-to-giant ratio was found. The primary purpose of these *Hubble Space Telescope* (*HST*) data were to study the morphologies and structural properties of the giants and dwarfs, and in particular to identify the nature of the population responsible for the apparently steep LF upturn at the faint end. An initial attempt in this regard, using ground-based data, was made by Boyce et al. (2001). They concluded that the population responsible for the faint upturn could be subdivided into three categories: a contaminating population of background high-redshift elliptical galaxies, an overdensity (relative to the giants) of dwarf elliptical galaxies, and an overdensity of dwarf irregular galaxies. The type classification was made on the basis of color. Boyce et al. (2001) noted that when the population of contaminating background galaxies was removed, the overall LF still showed a distinct upturn ($\alpha = -1.22$) and a generally high overdensity of dwarf galaxies. From the colors, it was concluded that the main component of this population was blue and therefore presumed to consist of dwarf Irregular galaxies. Furthermore, Boyce et al. (2001) argued that the core was devoid of dIrr's, which were mostly destroyed via processes such as galaxy harassment (Moore, Lake, & Katz 1998), thus accounting for the increase in the luminosity function faint-end slope from the center outward (Driver et al. 1998a).

The plan of this paper is as follows: In § 2, we summarize the observations, reduction, and analysis of the *HST* images. In § 3, we describe and validate the morphological classification process, and in § 4 we describe the appropriate error analysis incorporating the clustering signature of the background population. In § 5, we show the overall and morphological luminosity distributions, determined via statistical background subtraction, and compare them with recent field estimates to test BST88's hypothesis. In § 6, we investigate the radial distribution in terms of the luminosity- and number-density profile of each morphological type, and we conclude in § 7. We adopt $H_0 = 65\ \mathrm{km^{-1}s^{-1}Mpc^{-1}}$, $\Omega_M = 0.3$, and $\Omega_\Lambda = 0.7$ throughout, this results in a distance modulus to A868 of 39.47 mag (excluding *K*-correction).

2. DATA ACQUISITION, REDUCTION, AND ANALYSIS

A868 formed part of a cluster population study by Driver et al. (1998a), in which a high dwarf-to-giant ratio was found (see also Boyce et al. 2001). To pursue this further 12 orbits were allocated in cycle 8 with the WFPC2 onboard the *HST* to obtain a six-pointing F606W mosaic of the cluster. A868 lies at coordinates $\alpha = 09^{\mathrm{h}}45^{\mathrm{m}}26\overset{\mathrm{s}}{.}43$, $\delta = -08°39'06\overset{''}{.}7$, $z = 0.153$ (Strubble & Rood 1999). The cluster has an Abell richness class 3 and is of Bautz-Morgan type II–III (see Driver et al. 1998a and Boyce et al. 2001 for the earlier work on A868).

The data comprise 24 individual exposures of 1100 s, each targeted at six individual and marginally overlapping pointings (see Fig. 1). The data were combined using a pixel clipping algorithm based on local sky statistics developed

[2] It is worth noting that both studies used a fixed field-of-view size, limited by the respective detectors, and hence representing progressively larger physical extents for higher redshift clusters.

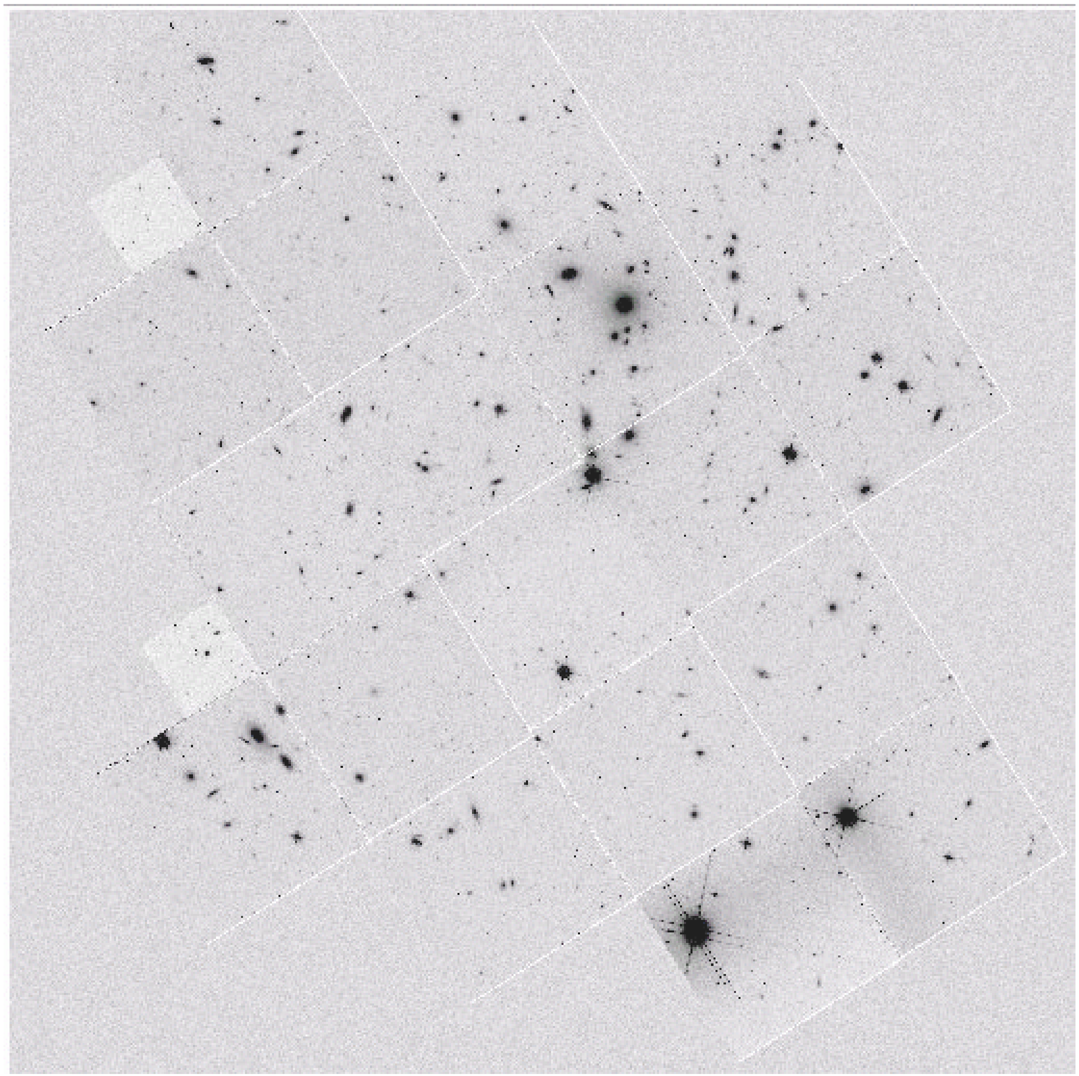

FIG. 1.—Full six-pointing mosaic of the A868 cluster and environs. North is up, with east to the left. The box is 6/62 (or 1.08 Mpc at $z = 0.158$) on each side. The cluster core is clearly visible and shown in more detail in Fig. 2.

for use with WFPC2 images in the LMORPHO package (Odewahn et al. 2002). Extensive tests were made comparing the photometry derived from such stacks with those derived from the DRIZZLE algorithm (Fruchter & Hook 2002) with no appreciable systematic difference found. The LMORPHO stacks, produced in a more straightforward fashion, and free of problems associated with correlated pixel noise, were adopted for further use. The final pixel scale is 0"0996 pixel^{-1} and the full mosaic field covers an area of 0.007545 deg^2. Figure 2 shows the WFPC2 chip containing the cluster core, showing the dominant cD and D galaxies and evidence for strong gravitational lensing. The photometric zero point for each mosaic was 30.443, as taken from Holtzmann et al. (1995), placing the photometry onto the Vega system. Initial object source catalogs were derived with SExtractor (Bertin & Arnouts 1996) using a 2 σ sky level threshold (per pixel) and a minimum isophotal area of 5 pixels. A GUI-based image editor in the LMORPHO package was used to visually inspect image segmentation over the field and edit obvious problems. Image postage stamps were prepared for each detected source and the GALPHOT package in LMORPHO was used to perform automated galaxy surface photometry. This package incorporates information about nearby cataloged sources and performs modest corrections designed to decrease photometric degradation from field crowding. The LMORPHO catalog for 1616 valid objects in A868 contained a variety of image structural parameters, as well as total magnitudes and quartile radii (including the effective radius)—for full details of the inner workings of this software package, see Odewahn et al. (2002). Note that final magnitudes are extinction corrected using Schlegel, Finkbeiner, & Davis (1998) dust maps. Briefly an initial isophotal magnitude within an elliptical aperture is measured and the data is corrected to total based upon the extrapolated profile fit. In most cases, this provides an excellent approximation to the total magnitude and is ideal for crowded sight lines such as A868. However, its well known that for anomalous and/or flat-profile objects the isophotal correction can become unrealistically large. As a check of the isophotal corrections, we show the isophotal versus total magnitudes for the full A868 galaxy population (see Fig. 3). Clearly a small fraction of objects do indeed have unrealistic isophotal corrections. We hence adopt a cap to the isophotal correction shown as

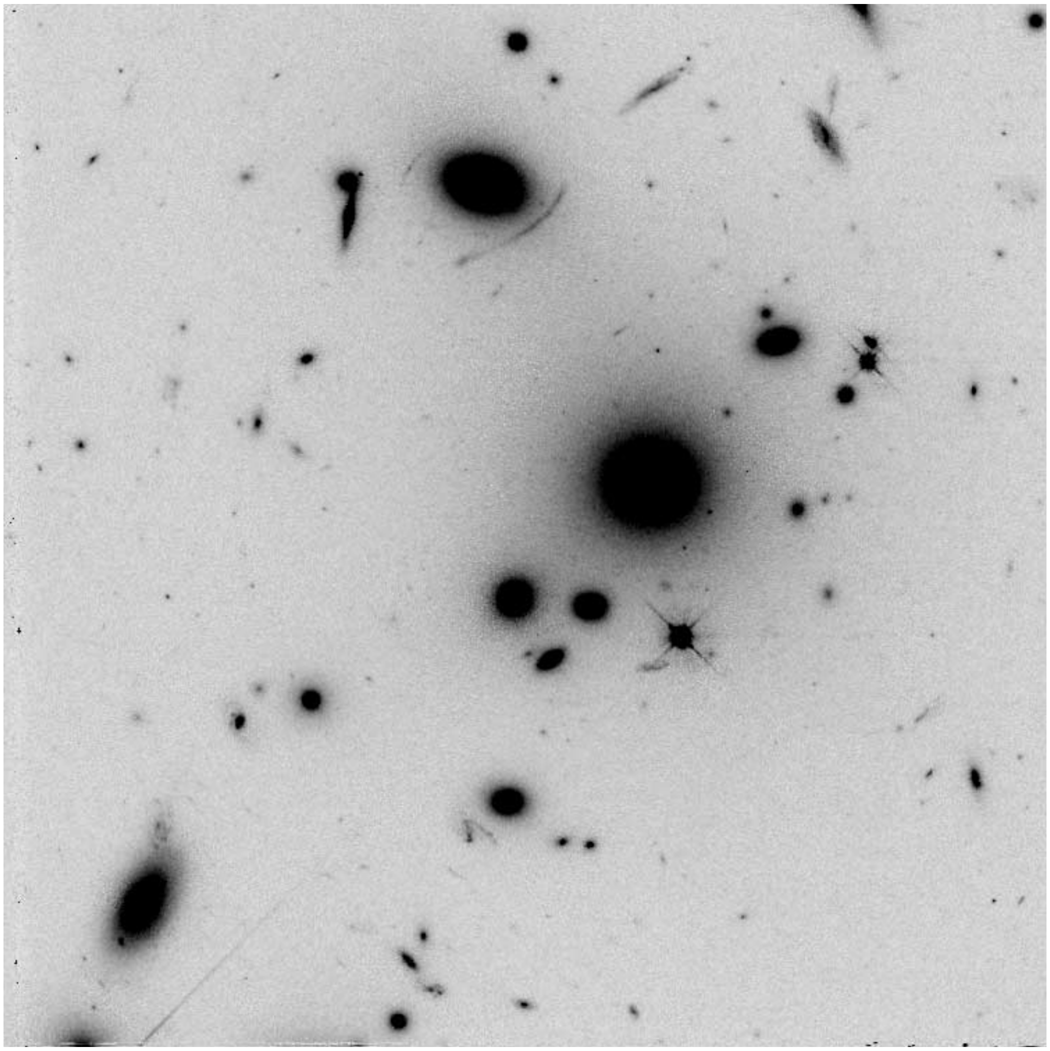

FIG. 2.—Single WFPC2 chip showing the core of the rich cluster A868. The image is approximately 1.5 on each side (0.25 Mpc). Clearly visible is the central cD and one of the D galaxies with numerous examples of gravitational lenses.

the dotted line. This is a simple power law fitted to the lower bound of the brighter data (note that not surprisingly the cap is only required for the late types, triangles in Figure 4, which exhibit nonstandard profile shapes). The expression for the isophotal cap is given by $m_{\rm Total} \leq m_{\rm Iso} + 0.25 - 0.0055(m_{\rm Iso} - 16)^{2.5}$.

Finally, Figure 4 shows the apparent bivariate brightness distribution, this highlights that stars and galaxies are well separated to $m_{\rm F606W} \leq 24.0$ mag, and that the bulk of the galaxy population lies above the surface brightness detection isophote to the same limit. From Figure 4, it is also apparent that earlier types are of higher effective surface brightness in line with conventional wisdom.

2.1. *Reference Field Counts*

In order to determine the contribution to the A868 galaxy counts from the field, we performed an identical reduction and analysis on the Hubble Deep Field North (HDF-N), Hubble Deep Field South (HDF-S), and the deep field 53W002 (Driver et al 1995; Windhorst, Keel, & Pascarelle 1998)—all observed in F606W, covering $\sim$0.0011 deg^2, and calibrated onto the same photometric system as A868 (see Cohen et al. 2003 for further details of these specific fields). However, these three deep fields only provide reference counts at faint magnitudes ($m_{\rm F606W} > 21$ mag). To provide reference counts at brighter magnitudes, we adopt the Millennium Galaxy Catalogue (MGC; Liske et al. 2003; Cross et al. 2003) and convert the MGC photometry from $B_{\rm MGC}$ to F606W. This is achieved by convolving the Isaac Newton Telescope's KPNO B and the *HST*'s F606W filter+instrument transmission functions with the mean zero-redshift cosmic spectrum from the 2dF Galaxy Redshift Survey (Baldry et al. 2002), after dividing out the equivalent flux-calibrated spectrum for Vega (see, for example, Sung & Bessell 2000). This resulted in a transformation of $(B_{\rm MGC} - {\rm F606W})_{\rm Vega} = +1.06$. Although the MGC counts extend to $B = 24$ mag, the color transformation above will only be appropriate for noncosmological distances, i.e., $B \leq 18.25$ mag.

3. GALAXY CLASSIFICATION

Object classification for the A868, HDF-N, HDF-S, and 53W002 fields were performed using an Artificial Neural

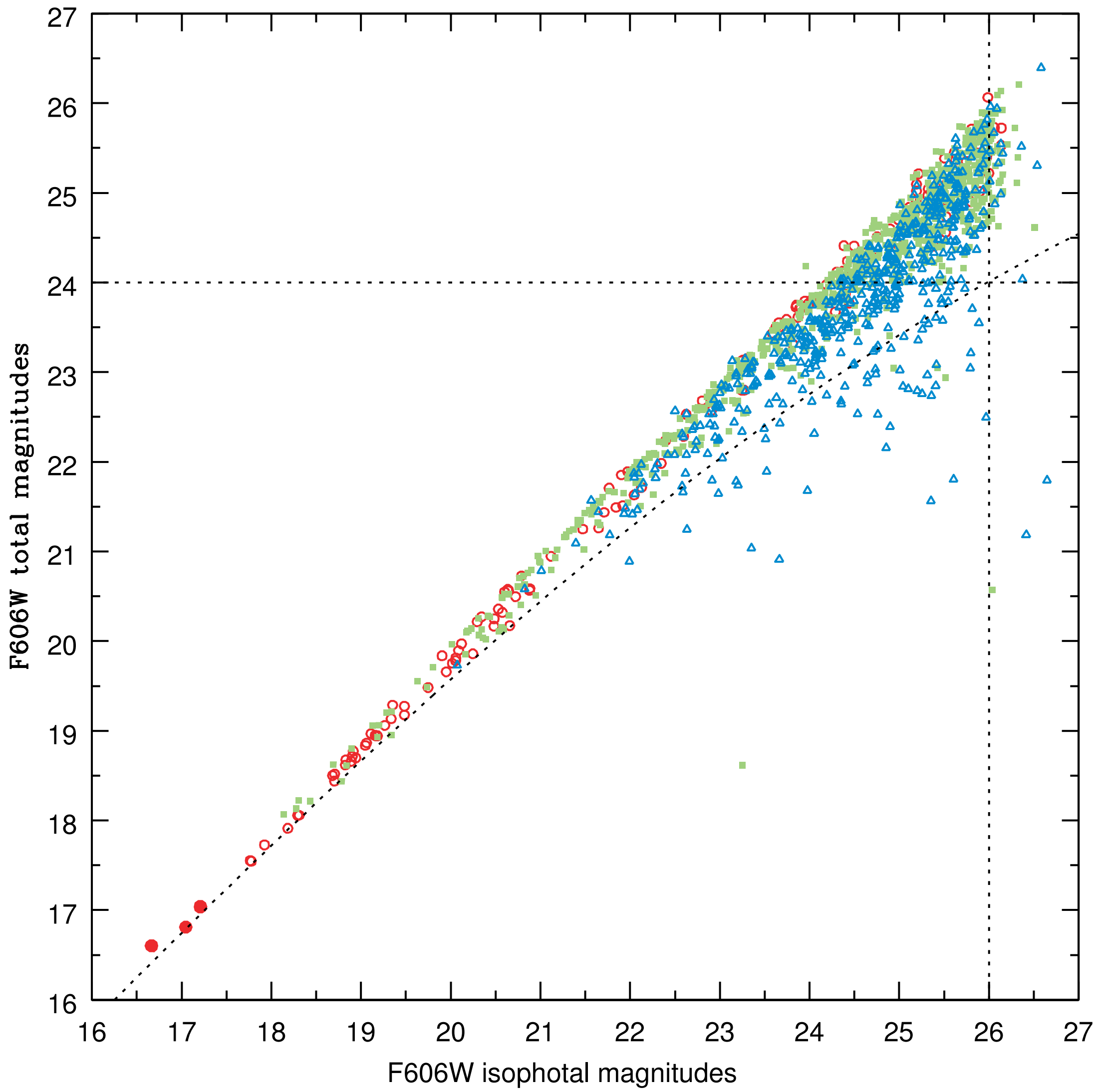

FIG. 3.—Total vs. isophotal magnitudes for the full A868 mosaic. The cD/D's and early , mid, and late types are denoted as filled circles, open circles, filled squares, and open triangles, respectively. The dotted line shows the adopted cap to the isophotal corrections. (Note that the one spiral furthest from the unity line lies close to a bright elliptical galaxy resulting in the extreme isophotal correction.)

Network (ANN), as described in Odewahn et al. (1996). Briefly, the ANNs were initially trained on a sample classified by eye, drawn from a variety of data sets including the *HST B*-Band Parallel Survey (BBpar) (Cohen et al. 2003) and RC3 catalogs (de Vaucouleurs et al. 1995). The ANNs take as input parameters a set of structural measurements for each image (seven isophotal areas and a seeing/point-spread function measurement) and output a classification onto the 16-step de Vaucouleurs' *t*-type system (see de Vaucouleurs et al. 1995) with an additional step added for stars. Stars are defined as *t*-type = 12, early types (E/S0) as $-6.0 \leq t$-type ≤ 0.0, mid types (Sabc) as $0.0 < t$-type ≤ 6.0, and late types (Sd/Irr) as $6.0 < t$-type ≤ 10.0. An error is allocated to each classification based upon the dispersion among five independently trained ANNs. As a check of the classification accuracy, we visually inspected all objects brighter than $m_{\mathrm{F606W}} < 24.0$ mag. In 80 out of the 663 cases, a visual override was necessary. The majority of these were due to entangled isophotes (i.e., crowding), which is known to cause some problems with ANN classifications. Table 1 summarizes the overrides and no obvious classification bias is apparent. We also note that three of these errors were the A868 central cD and two D galaxies which were all erroneously classified as Sabc's. As no cD or D galaxies were included in the ANN training sets, it is understandable that the giant bulge surrounded by a low surface brightness halo could readily be confused with a mid-type spiral. Excluding these three specific objects,

TABLE 1
SUMMARY OF MORPHOLOGICAL CLASSIFICATION OVERRIDES

Type	Ellipticals	Early Types	Late Types	Stars
Ellipticals........	. . .	4	0	2
Early types......	2	. . .	20	0
Late types	1	32	. . .	0
Stars................	2	3	1	. . .
Junk................	2	11	2	6

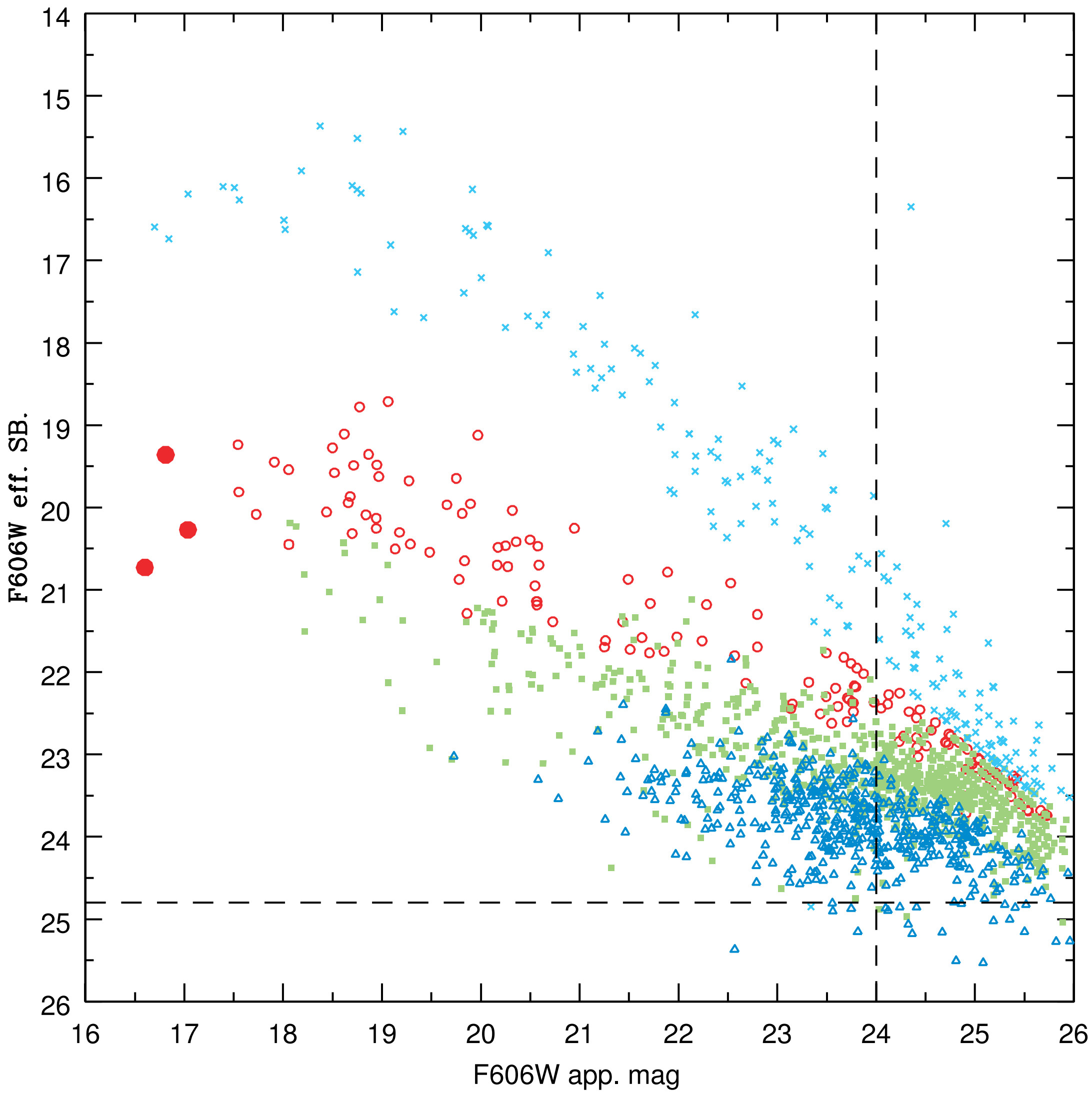

FIG. 4.—Apparent bivariate brightness distribution for galaxies in the A868 sight-line. The effective surface brightness is derived from the measured major-axis half-light radius ($\mu_{\rm eff} = m + 2.5\log_{10}(2\pi r_{\rm hlr}^2)$). Large filled circles denote cD/D's, open circles early types, filled squares mid types, triangles late types, and crosses stars. The dashed lines denote the limiting surface brightness and star-galaxy separation limit.

thereby gives an unchecked ANN classification accuracy of ~90%. Postage-stamp images for randomly selected galaxies are shown in Figure 5, ordered by type and apparent magnitude.

For the ground-based MGC data all galaxies brighter than $B \leq 18.25$ were classified by eye (S. C. O.) to provide fully consistent[3] bright magnitude reference counts.

4. ERROR ANALYSIS

Prior to field subtraction, it is first worth making careful consideration of the error budget, particularly in light of concerns raised by Valotto et al. (2001) that many of the steep faint ends observed in clusters, are due to the clustering signature of the background field population. This has some justification as the error analysis involved when subtracting reference counts from cluster counts has often been overlooked (for example, in Driver et al. 1994). Here we intend to extend the normal analysis to now incorporate this additional error component.

In this particular analysis, there are five components to the error budget: Counting errors occur in the reference counts (σ_R), the field counts in the cluster sight-line (σ_F), and the cluster population itself (σ_C), along with the clustering error in the two sets of field counts (ψ_R and ψ_F). Note that we separate out the two counting errors in the cluster sight-line since in reality there are two distinct superposed populations (field, F and cluster, C). For all three counting errors, we adopt the usual assumption of $\sqrt{n}$ statistics for the associated error (i.e., Poisson statistics). For the clustering error, we start from the prescription given in Peebles (1980, equation [45.6]) which provides an expression for the total variance in cell-to-cell counts for a randomly placed cell as

$$\langle (N - n\Omega)^2 \rangle = n\Omega + n^2 \int d\Omega_1 d\Omega_2 \omega(\theta_{12}) \ . \qquad (1)$$

[3] This process produces fully consistent counts as the ANNs were trained on data classified by S. C. O.

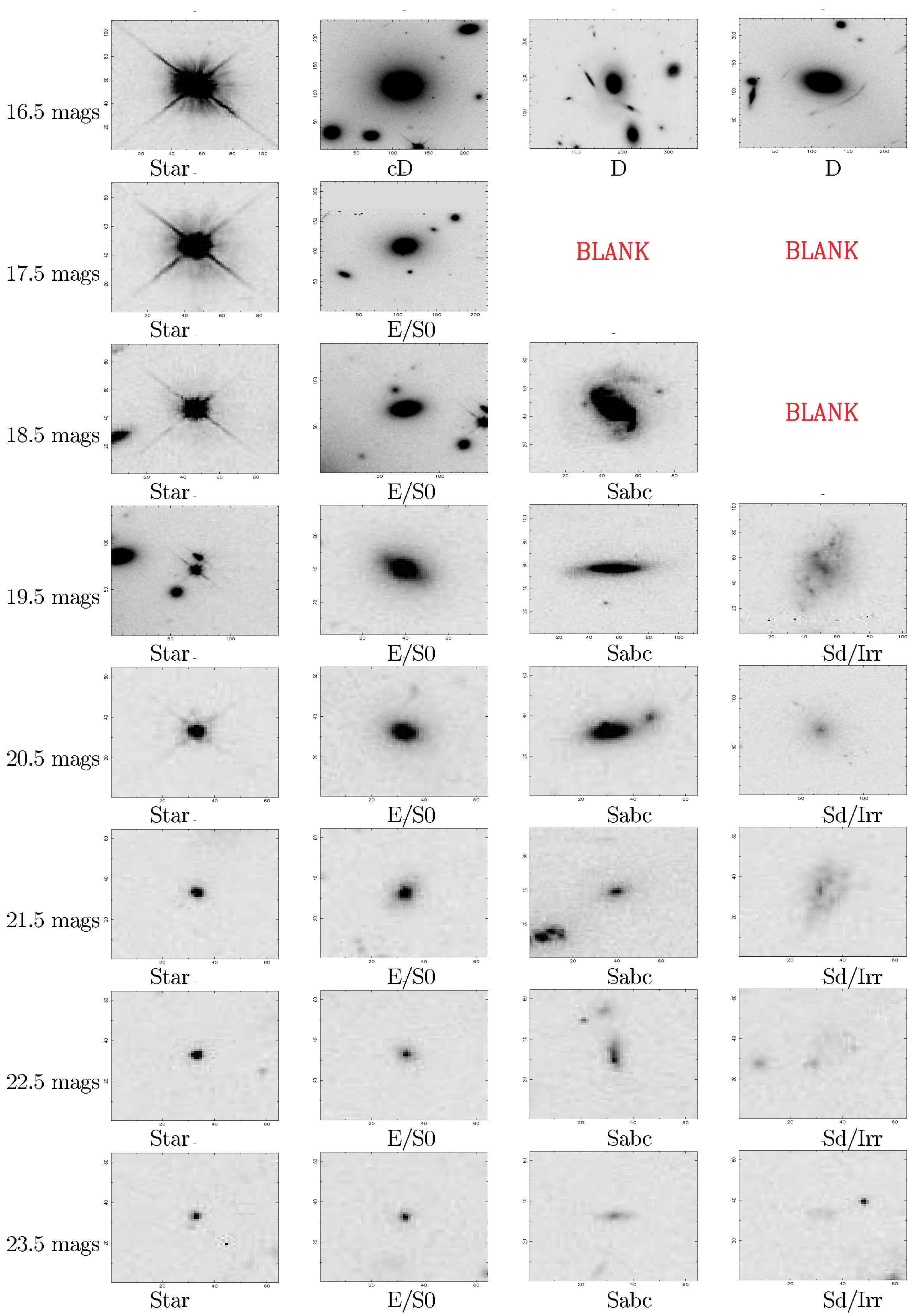

FIG. 5.—Random sample of stars, early, mid, and late types (*across*) vs. apparent magnitude (*down*)

Here N is defined as the counts in a given cell (i.e., per field-of-view, Ω), n is the global mean count per square degree, and θ_{12} is the separation between the solid angle elements $d\Omega_1$ and $d\Omega_2$. In this expression, the first term represents the Poisson error (σ) and the second the clustering error (ψ), i.e.,

$$\sigma^2 = n\Omega \ , \tag{2}$$

$$\psi^2 = n^2 \int d\Omega_1 d\Omega_2 \omega(\theta_{12}) \ , \tag{3}$$

$$\approx n^2\theta^4\omega(\sqrt{2}\theta/3) \ , \tag{4}$$

$$= n^2 A_w \theta^{3.2}(\sqrt{2}/3)^{-0.8} \ . \tag{5}$$

The above simple approximation for ψ uses the mean separation between points in a square of side θ (Phillipps & Disney 1985) and the standard expression for the angular correlation function of $\omega(\theta) = A_w\theta^{-0.8}$. Replacing $n\Omega$ with $N(m)$ (the number counts for the specified field of view) and A_w with $A_w(m)$ yields the variances from the clustering error for any field size (Ω or θ^2) and magnitude interval (m). Observationally, we find (Roche & Eales 1999) that

$$A_w(m) = 10^{-0.235m_r+2.6} \ . \tag{6}$$

Hence by combining equations (5) and (6) and adopting (F606W$-R$) = 0.2–0.6, we obtain a final approximation for ψ of

$$\psi^2 \approx 1.83N(m_{\rm F606W})^2 10^{(-0.235m_{\rm F606W}+2.7)}\Omega^{-0.4} \ . \tag{7}$$

Assuming ω remains a power law out to the size of the field. Here $N(m_{\rm F606W})$ are the galaxy counts per 0.5 mag for the specified field of view, Ω, which is given in square degrees.

The five errors identified above can now be written down explicitly as follows:

$$\sigma_R = (\sqrt{N_R}\Omega_C)/3\Omega_R \ , \tag{8}$$

$$\psi_R = \sqrt{1/3[1.83(N_R/3)^2 10^{(-0.235m+2.7)}\Omega_R^{-0.4}]}(\Omega_C/\Omega_R) \ , \tag{9}$$

$$\sigma_C = \sqrt{N_C} \ , \tag{10}$$

$$\sigma_F = \sqrt{N_F} \ , \tag{11}$$

$$\psi_F = \sqrt{[1.83(N_F)^2 10^{(-0.235m+2.7)}\Omega_C^{-0.4}]} \ , \tag{12}$$

where N_R, N_F, and N_C are the number counts for the combined reference fields, the field population in the A868 sight-line and the number counts of the cluster population respectively, and Ω_R and Ω_C are the fields of view of the three individual reference fields (0.0011 deg^2) and the cluster field of view (0.007545 deg^2), respectively. Where appropriate these errors, or their adaptations, are combined in quadrature and used throughout all further analysis steps.

5. THE MORPHOLOGICAL LUMINOSITY DISTRIBUTIONS OF A868

The overall and morphological galaxy number counts for the full A868 mosaic and the combined reference fields scaled to the same area are shown on Figure 6. Note that the A868 total counts lie above the reference field counts until $m_{\rm F606W} \approx 24.25$ (and for each class until $m_{\rm F606W}^{\rm E/S0} \approx 25.25$, $m_{\rm F606W}^{\rm Sabc} \approx 24.75$, and $m_{\rm F606W}^{\rm Sd/Irr} \approx 24.0$), at which point the A868 counts drop sharply indicating the approximate completeness limit(s) of the A868 data (see also Fig. 4). We hereby adopt $m_{\rm F606W} \approx 24$ mag as the completeness limit (equivalent to $M_{\rm F606W} = -16$ mag) and 0.75 mag brighter than the apparent completeness limit. The reference counts, obtained from the two Hubble Deep Fields and 53W002, extend substantially deeper than the A868 counts but provide no available data at bright magnitudes ($m_{\rm F606W} < 21$ mag). To circumvent this, we add in the MGC bright counts after transposing from B to F606W as discussed in § 3. To provide continuous coverage over the full magnitude range, we now elect to represent the field counts by a second-order polynomial fit[4] to the combined reference field data. As well as providing continuous coverage, this has the additional advantage of smoothing the reference data to remove unwanted structure from the three contributing fields. The field data used and the resulting fits are shown in Tables 2 and 3, respectively. Note that the data were only fitted over the magnitude range $15.75 < m_{\rm F606W} < 24.25$, although additional data are shown in Table 2 for completeness. The smoothing of the counts does not reduce the associate errors but redistributes it over the specified magnitude range.

Subtracting the smoothed reference field counts from the A868 counts for each population yields a direct statistical representation of the morphological luminosity distribution for the cluster (adopting a universal Sab K-correction of 0.20 mag), as shown on Figure 7 and tabulated as Table 4. Also shown on Figure 7 (*top left*, *dotted line*) is the 2dFGRS composite cluster LF as derived by De Propris et al. (2003), shifted to the F606W bandpass. This gives a formally acceptable fit to the cluster. The open squares show the previous and deeper ground-based R-band data, which agrees well within the errors. Given that the background subtraction is derived from an entirely different region of sky to the earlier work (see Driver et al. 1998a), this provides a further indication that the steep faint-end slope seen in A868 is a robust result. Of course, one might argue that the A868 sight-line could be contaminated by a more distant cluster, although this would boost the faint elliptical counts/LF which is not seen. Figure 7 shows the LFs of elliptical (E/S0's, *top right*), spiral (Sabc's, *bottom left*), and irregular (Sd/Irr's, *bottom right*). Morphological K-corrections of K(E/S0) = 0.25, K(Sabc) = 0.20, and K(Sd/Irr) = 0.11 were calculated for the F606W filter combined with the 15 Gyr evolved E, Sa, and Sc model spectra of Poggianti (1997). The formal 1, 2, and 3 σ error ellipses for the Schechter function fits, based on the χ^2 minimization of the standard Schechter LF, are shown as Figure 7. The results and formal 1 σ errors are also tabulated in Table 5. For Figure 7 (*top left*, all types), the solid line shows the sum of the three individually derived morphological LFs showing interesting structure consistent with recent reports of an upturn at fainter magnitudes (e.g., A0963; Driver et al. 1994) and/or a dip at intermediate magnitudes (e.g., Coma, Trentham 1998). If each morphological class has a universal LF, as has been suggested (BST88), this dip then naturally arises as the morphological mix changes (as required by the morphology-density relation, Dressler et al. 1997). The error bars shown in Figure 7, and the resulting error contours shown on Figure 8, include the five error components discussed in § 4. It is worthwhile assessing which of these

[4] The fit is a least-squares fit to the data with the errors given by equations (8) and (9).

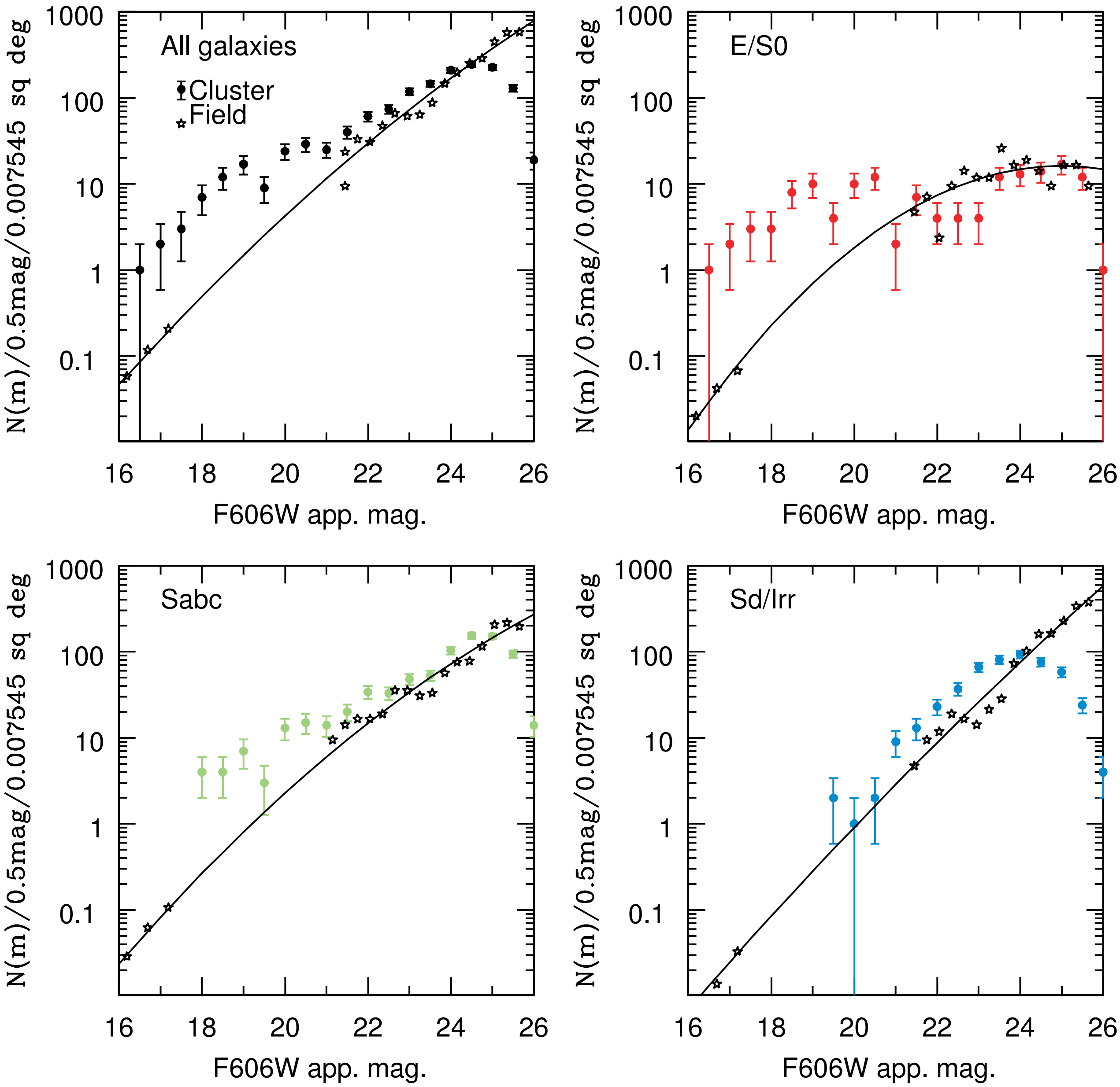

FIG. 6.—Cluster sight-line and reference field counts (scaled to the A868 field-of-view size of 0.007545deg^2). Counts are shown for all galaxies together and early, mid, and late types separately. The solid lines shows a second-order polynomial fit to the field count data. Errors are purely Poisson at this point.

error components dominate the error budget. Figure 9 shows the total and individual error components involved in this analysis. From this figure, we can see that the dominant error at bright magnitudes comes from the number of cluster members, whereas at faint magnitudes the dominant error typical comes from the clustering of the background population in the cluster sight-line. One interesting point to note is that a full blown spectroscopic study would fail to reach the faint magnitudes probed here, and of course be unable to improve the statistics at bright magnitudes. In fact, a spectroscopic study is more likely to lead to additional uncertainty due to completeness issues. Further improvement can only come from the combination of extensive deep *imaging* data for a large sample of combined cluster data. Nevertheless, it is clear from Figure 7 that the steep faint end seen in A868 is almost entirely dominated by late types with some contribution from mid types in general agreement with the findings of Boyce et al (2001).

5.1. *Comparisons with the Field*

Unfortunately, while field morphological LFs exist, no comparison is sensible unless an identical morphological classification methodology has been applied. However, as a general result, morphological field studies typically find $\alpha > -1$ for early types, $\alpha \approx -1$ for mid types, and $\alpha < -1$ for late types (see, for example, SSRS2's morphological LFs, Marzke et al. 1998; 2dFGRS's spectral LFs, De Propris et al. 2003, Madgwick et al. 2002; and SDSS-EDR's morphological LFs, Nakamura et al. 2003). We compare the recent results, from the SDSS-EDR, who classify 1500 galaxies onto a similar but not identical

TABLE 2

NUMBER COUNT DATA FOR ALL EARLY-, MID-, AND LATE-TYPE REFERENCE FIELD GALAXIES PER 0.007545 DEG^2

Magnitude	N(All)	N(E/S0)	ΔN(Sabc)	ΔN(Sd/Irr)
15.190	0.016 ± 0.003	0.003 ± 0.001	0.010 ± 0.002	0.003 ± 0.001
15.690	0.030 ± 0.005	0.011 ± 0.002	0.012 ± 0.003	0.006 ± 0.002
16.190	0.057 ± 0.009	0.020 ± 0.004	0.028 ± 0.005	0.009 ± 0.002
16.690	0.115 ± 0.015	0.041 ± 0.006	0.060 ± 0.008	0.013 ± 0.002
17.190	0.202 ± 0.023	0.066 ± 0.008	0.104 ± 0.012	0.032 ± 0.004
21.450	23.003 ± 8.751	4.601 ± 3.395	9.201 ± 5.061	4.601 ± 3.395
21.750	32.204 ± 10.655	6.901 ± 4.205	13.802 ± 6.346	9.201 ± 4.938
22.050	29.904 ± 9.886	2.300 ± 2.337	16.102 ± 6.849	11.502 ± 5.544
22.350	46.006 ± 12.811	9.201 ± 4.847	16.102 ± 6.740	18.402 ± 7.187
22.650	64.409 ± 15.664	13.802 ± 6.018	18.402 ± 7.187	16.102 ± 6.566
22.950	59.808 ± 14.452	11.502 ± 5.394	34.505 ± 10.357	13.802 ± 5.962
23.250	62.108 ± 14.432	11.502 ± 5.357	34.505 ± 10.154	20.703 ± 7.409
23.550	85.111 ± 17.329	25.303 ± 8.212	29.904 ± 9.162	27.604 ± 8.631
23.850	142.619 ± 24.035	16.102 ± 6.342	32.204 ± 9.436	71.309 ± 15.048
24.150	190.925 ± 28.632	18.402 ± 6.773	55.207 ± 12.822	98.913 ± 18.157
24.450	246.133 ± 33.231	13.802 ± 5.783	73.610 ± 15.030	156.421 ± 24.024
24.750	280.637 ± 35.223	9.201 ± 4.670	75.910 ± 15.027	158.721 ± 23.569
25.050	437.058 ± 47.259	16.102 ± 6.221	112.715 ± 18.849	220.829 ± 28.661
25.350	558.974 ± 54.724	16.102 ± 6.201	200.127 ± 26.792	331.244 ± 36.906
25.650	565.875 ± 52.836	9.201 ± 4.643	211.628 ± 27.051	365.748 ± 38.259

NOTE.—The errors include both Poisson and clustering components.

TABLE 3

SECOND-ORDER POLYNOMIAL FITS TO THE FIELD NUMBER-COUNT DATA OVER THE RANGE $15 < m < 24.25$

Fit	χ^2	ν
$\log N(\mathrm{All})dm = -14.752 + 1.103m_{\mathrm{F606W}} - 0.0166m^2_{\mathrm{F606W}}$	7.8	12
$\log N(\mathrm{E/S0})dm = -18.595 + 1.484m_{\mathrm{F606W}} - 0.0273m^2_{\mathrm{F606W}}$	10.0	11
$\log N(\mathrm{Sabc})dm = -16.770 + 1.290m_{\mathrm{F606W}} - 0.0215m^2_{\mathrm{F606W}}$	10.0	12
$\log N(\mathrm{Sd/Irr})dm = -11.491 + 0.639m_{\mathrm{F606W}} - 0.0035m^2_{\mathrm{F606W}}$	14.2	11

TABLE 4

ESTIMATED CLUSTER POPULATION FOR ALL EARLY-, MID-, AND LATE-TYPE A868 CLUSTER GALAXIES PER 0.007545 DEG^2

Magnitude	N(All)	N(E/S0)	N(Sabc)	N(Sd/Irr)
16.00	−0.05 ± 1.07	−0.01 ± 1.02	−0.02 ± 1.04	−0.01 ± 1.01
16.50	0.91 ± 1.10	0.97 ± 1.03	−0.05 ± 1.07	−0.01 ± 1.02
17.00	1.84 ± 1.55	1.94 ± 1.46	−0.09 ± 1.14	−0.02 ± 1.04
17.50	2.70 ± 1.94	2.89 ± 1.80	−0.16 ± 1.25	−0.04 ± 1.07
18.00	6.46 ± 2.90	2.81 ± 1.86	3.70 ± 2.18	−0.08 ± 1.13
18.50	10.03 ± 3.69	7.67 ± 2.97	2.47 ± 2.09	−0.14 ± 1.22
19.00	15.32 ± 4.67	9.43 ± 3.38	6.07 ± 3.07	−0.26 ± 1.37
19.50	5.13 ± 4.08	3.06 ± 2.52	1.42 ± 2.69	0.54 ± 1.46
20.00	18.19 ± 6.20	8.51 ± 3.72	10.38 ± 4.51	−0.83 ± 1.96
20.50	20.10 ± 7.43	9.69 ± 4.25	10.75 ± 5.23	−0.47 ± 2.48
21.00	7.25 ± 8.20	−1.46 ± 3.71	8.29 ± 5.95	0.40 ± 3.12
21.50	17.84 ± 10.89	1.97 ± 4.55	9.67 ± 7.26	6.41 ± 4.83
22.00	30.70 ± 14.03	−3.09 ± 5.25	20.47 ± 9.34	13.94 ± 6.69
22.50	21.34 ± 17.02	−5.67 ± 6.12	10.23 ± 10.52	17.90 ± 8.61
23.00	39.80 ± 21.54	−8.79 ± 7.02	12.44 ± 12.63	37.43 ± 11.88
23.50	55.65 ± 26.65	−4.38 ± 7.92	10.57 ± 14.81	49.35 ± 15.55
24.00	66.95 ± 32.43	−7.34 ± 8.78	42.17 ± 18.15	26.27 ± 19.69

NOTE.—The errors include both Poisson and clustering components.

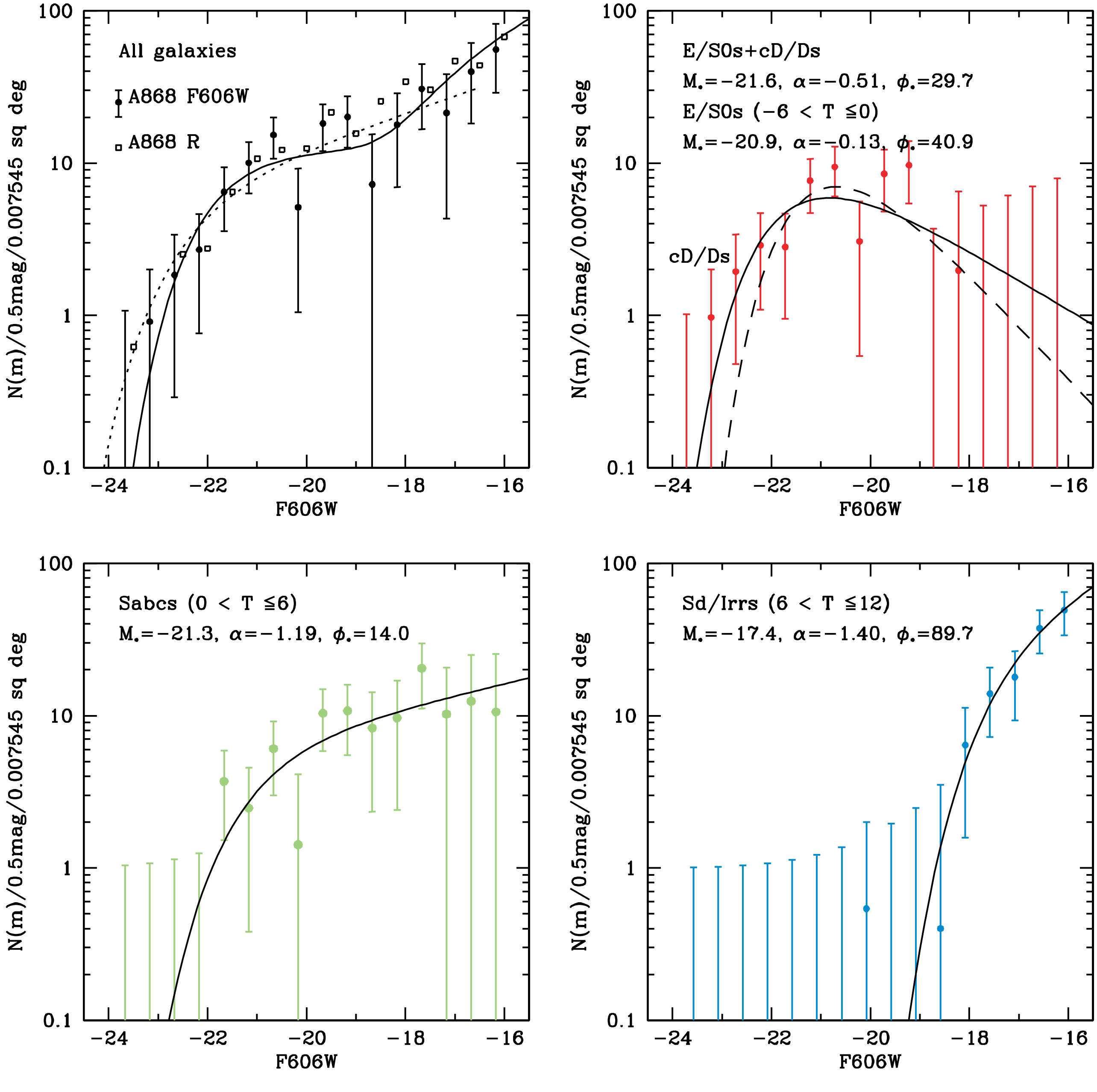

FIG. 7.—Recovered luminosity distributions for the cluster population after subtracting the reference field counts from the A868 sight line counts. The error bars now include the full error analysis (i.e., five error components including three Poisson and two clustering errors). The solid lines show the χ^2-minimized Schechter function fits to the data. In the case of all galaxies, we also show the 2dFGRS composite cluster luminosity function (De Propris et al. 2003) transposed to the F606W filter and renormalized to match the data. The squares show the previous deeper R-band cluster results from Driver et al. (1998a).

TABLE 5

DERIVED SCHECHTER FUNCTION PARAMETERS FOR THE OVERALL AND MORPHOLOGICAL LUMINOSITY DISTRIBUTIONS OF THE RICH CLUSTER ABELL 868

Morphological Class	T-Type Range	$\phi_* h_{0.65}^3$ (0.007545 deg^{-2})	$M^*_{\rm F606W} - 5\log h_{0.65}$ (mag)	α	χ^2	ν
All................................	$-6 < T < 9$	16.4	$-22.4^{+0.6}_{-0.6}$	$-1.27^{+0.13}_{-0.15}$	8.8	12
E/S0+cD/D................	$-6 < T \leq 0$	29.2	$-21.6^{+0.6}_{-0.5}$	$-0.51^{+0.2}_{-0.3}$	7.9	7
E/S0	$-6 < T \leq 0$	41.2	$-20.9^{+0.4}_{-0.4}$	$-0.13^{+0.4}_{-0.4}$	6.9	5
Sabc.............................	$0 < T \leq 6$	14.0	$-21.3^{+1.0}_{-0.9}$	$-1.19^{+0.2}_{-0.2}$	6.0	10
Sd/Irr	$6 < T \leq 9$	89.7	$-17.4^{+0.7}_{-0.7}$	$-1.40^{+0.6}_{-0.5}$	0.7	4

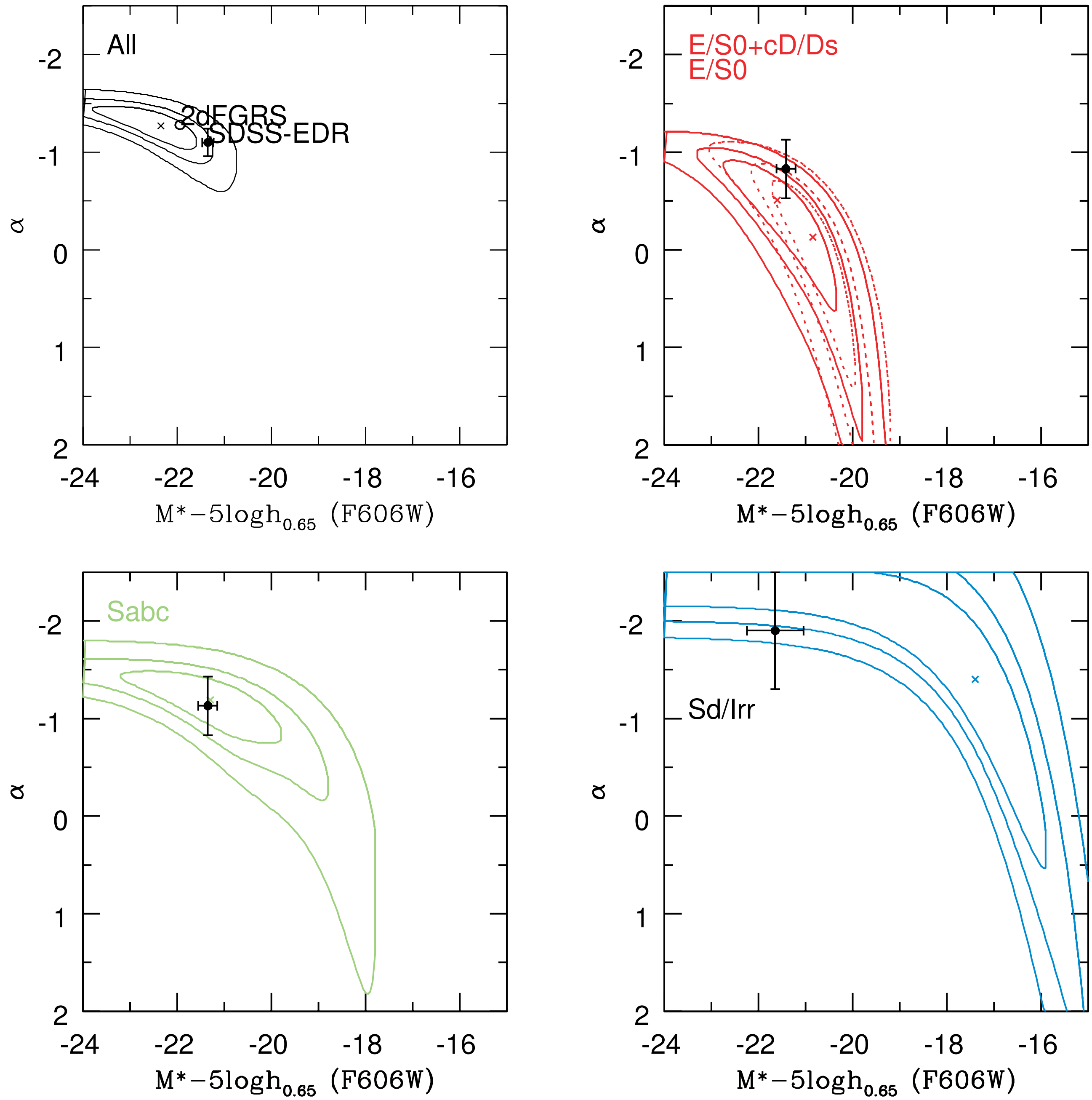

FIG. 8.—The 1, 2, and 3 σ error contours for the Schechter function fits shown in Fig. 9. The crosses shows the actual best-fit points. The solid points with error bars show the recent field estimates based on SDSS-EDR data by Nakamura et al. (2003). The open data point shows the recent composite cluster LF estimated from the 2dFGRS (De Propris et al. 2003), and errors are comparable to the symbol size. For the elliptical galaxies, the solid contours show the fit to E/S0's+cD/D's, and the dotted contours the fits to E/S0's only.

morphological system in r'. To adapt Nakamura et al.'s numbers to provide consistent morphological LFs, we added two-thirds of their Sbc–Sd class to their S0a–Sb class and one-third of their Sbc–Sd class to their Im class and rederived the Schechter function parameters. We also derive $(\mathrm{F606W}-r') = r' + 1.35(B-V) - 0.95$ (from Fukugita et al. 1996; Liske et al. 2003; and our estimate of $B_{\mathrm{MGC}}-\mathrm{F606W}$ from § 2.1) and adopt $(B-V)_{\mathrm{E/S0}} = 0.9$, $(B-V)_{\mathrm{Sabc}} = 0.7$, and $(B-V)_{\mathrm{Sd/Irr}} = 0.5$ (see Driver et al. 1994). This gives the following morphological field LFs:

1. $M^*_{\mathrm{E/S0}} = -21.42$, $\alpha_{\mathrm{E/S0}} = -0.8$;
2. $M^*_{\mathrm{Sabc}} = -21.35$, $\alpha_{\mathrm{Sabc}} = -1.1$; and
3. $M^*_{\mathrm{Sd/Irr}} = -21.65$, $\alpha_{\mathrm{Sd/Irr}} = -1.9$.

The location of the morphological field LFs are shown on Figure 8 as filled symbols with error bars. We see that the E/S0, Sabc, and Sd/Irr field and cluster LFs are all consistent at the 1 σ level (and in qualitative agreement the field and cluster LFs of BST88). Clearly though, the errors dominate and many clusters must be studied in a combined analysis before the universality of morphological luminosity functions can be confirmed or refuted. Given the extensive SDSS-EDR database and the incoming ACS cluster data, this is likely to be established in the near future and the current results should be taken as indicative that the

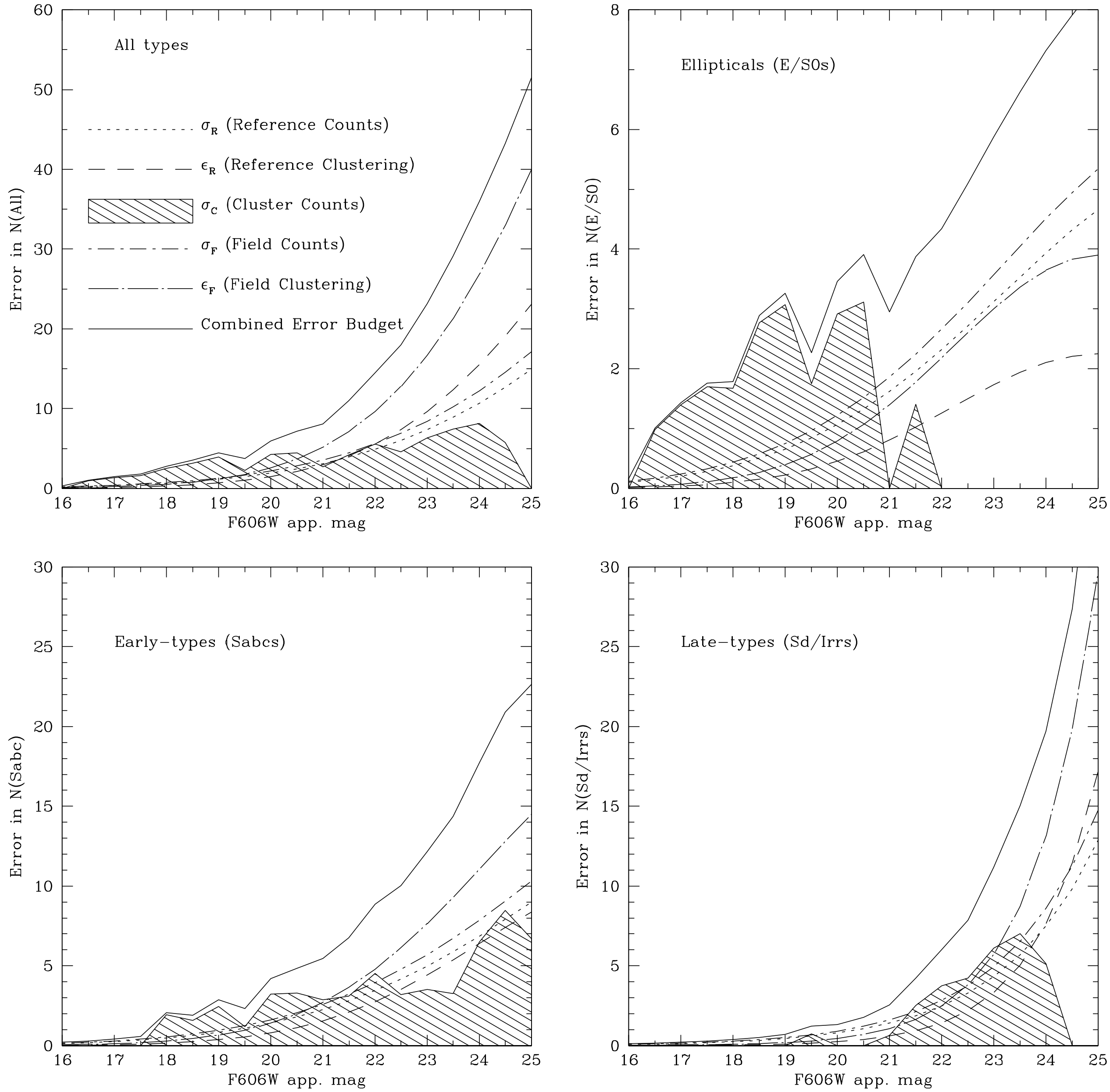

FIG. 9.—Five error components to the cluster luminosity distributions for all galaxies together and elliptical, early-type, and late-type galaxies separately. In most cases, the Poisson error in the cluster population dominates at brighter magnitudes, and the clustering error in the field population dominates at faint magnitudes.

morphological LFs are not widely variant between cluster and field environments.

6. THE MORPHOLOGICAL RADIAL DISTRIBUTIONS OF A868

We now subdivide the mosaic into five radial intervals of 0′.75 (130 kpc) around the dominant cD and calculate the contribution of each morphological class to the luminosity and number density within the range $15.9 < m_{\rm F606W} < 23.9$ mag (equivalent to $-24 < M_{\rm F606W} < -16$ mag). To achieve this, we build a map of the mosaic to calculate the relevant active fields of view, within each annulus, and use the expressions given in Table 3 to subtract off the appropriate field component. Figure 10 (*top*) shows the radial dependency of the luminosity density, j, for each type in arbitrary units and Figure 10 (*bottom*) the number density. Whereas the former is skewed toward brighter systems (which dominate the luminosity density), the latter is skewed toward fainter systems (at least for mid- and late-type spirals, which have rising LFs). From Figure 10, we find a number of indicative results. First though, we note the rise in luminosity density and number density in the final radial bin. This is likely because of the presence of the second D galaxy, which lies 0.7 Mpc from thecentral cD and may represent an infalling subgroup. Ignoring the bias introduced by this last bin, we find that the luminosity density of each class falls in a near linear fashion in $\log j$ versus radius with gradients of -0.68 ± 0.06, -0.32 ± 0.06, and -0.30 ± 0.18, for E/S0+ cD/D, Sabc, and Sd/Irr, respectively. Ignoring the cD/D

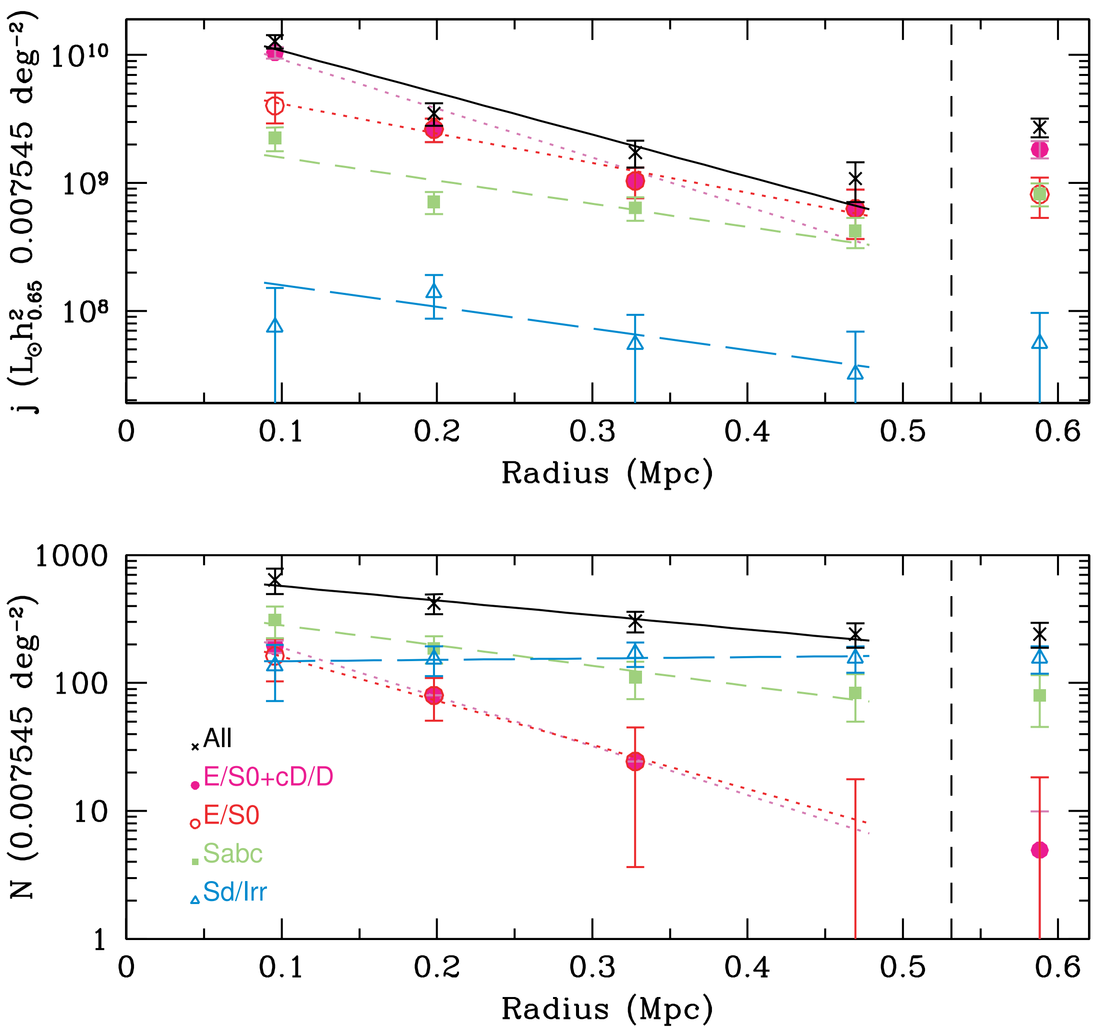

FIG. 10.—(*Top*) Luminosity-density profiles derived from the absolute magnitude range $-24 < M_{\rm F606W} < -16$ for all galaxies (*crosses*, *solid line*), cD/D+E/S0 (*pentagons*, *dotted line*), E/S0 (*circles*, *dotted line*), Sabc (*squares*, *short dashed*), Sd/Irr (*triangles*, *long dashed line*) in arbitrary units in five annuli centered around the central cD galaxies. (*Bottom*) Equivalent number-density profiles labeled as above.

galaxies results in a gradient of -0.41 ± 0.08 for the E/S0's alone (i.e., consistent with the mid-type population). This is, of course, an independent confirmation of the well-known morphology-density relation (Dressler et al 1997). Note that the exclusion of the cD/D's has little impact upon the derived Schechter function for early types (c.f. dashed line in Fig. 8, middle, E/S0's; see also Table 5). Similarly, the number densities also fall near linearly in log N versus radius with a significant variation in gradient depending on type (-0.68 ± 0.21, -0.28 ± 0.08, and $+0.02 \pm 0.07$, for E/S0+cD/D's, Sabc's, and Sd/Irr's, respectively).[5]

From Figure 10, two clear conclusions can be drawn. First, the classical result implies that early-type galaxies are more centrally concentrated in number than mid-type spirals, which in turn are more centrally concentrated than late-type irregular galaxies. Second, the flat number-density profile of late types implies that the core must be devoid of late types, which therefore exist exclusively in the cluster halo, independently confirming the result of Boyce et al. (2001). This halo extends beyond the field of view studied here, but from the luminosity-density profile, it is unlikely to contribute significantly to the total luminosity density at any radii. Within the field of view studied, we note that the total luminosity density, within all annuli, is divided into 72% $\pm$ 13% E/S0+cD/D's, 26% $\pm$ 3% Sabc's, and 2% $\pm$ 1% Sd/Irr's. This can be compared with those derived from the SDSS-EDR field LFs shown above (where $j = \phi^* L^* \Gamma(\alpha + 2)$) of 29%, 59%, and 12% for early, mid, and late types, respectively. Neglecting the cD/D's changes the cluster percentages to 63%, 34%, and 3%, respectively (with similar errors).

As a comparison, we note that values of 33%, 53%, and 14% for the field were derived by Driver (1999) for a volume-limited sample at $z \approx 0.45$ drawn from the Hubble Deep Field and classified using the same ANN classifiers as used here. The consensus between these two independent field studies is reassuring and provides some indication of the associated errors. If one assumes that both the field and cluster environments originate from an identical shape primordial mass spectrum but with differing amplitudes, this discrepancy *must* be due to an additional/accelerated

[5] Note that a projected profile with $\rho \propto r^{-k}$ is roughly equivalent to a real profile of $\rho \propto r^{-1-k}$, hence the positive projected profile for Sd/Irr's still implies a decreasing three-dimensional radial profile.

evolutionary mechanism(s) over those at work in the field. From this data alone, one cannot argue factually for the exact nature of this mechanism other than it has the *net* effect of converting later types toward earlier types and is most efficient in the cluster core. In fact, if one crudely adopts conservation of luminosity (strictly more valid at longer wavelengths) then up to 50% of the elliptical galaxies must have been formed from mid- or late-type spirals. This requires some contrivance given the apparent universality of the morphological LFs between the field and A868 environment, although far more data for both field and clusters are required before any real significance can be attached to the difference seen, as well as a more fully consistent classification scheme.

In general, the results here are consistent with the conventional picture whereby the core environment is hostile to disks and converts mid types to early types—which remain captured in the core—and destroys late types entirely as they transit through the core.

7. CONCLUSIONS

We report the first reconstruction of morphological luminosity functions for a cluster environment since the founding work of BST88. Through the method of background subtraction, we recover the overall LF seen for A868 in a previous ground-based study, but which used an entirely different region of sky for the background subtraction; this adds credence to the methodology of background subtraction for this very rich cluster at least. In our analysis, we lay down a methodology for accounting for background clustering bias missing in previous analysis of this type and addressing concerns raised by Valotto et al. (2001).

The overall cluster LF is comparable to the general field LF (2dFGRS) and we find that the early-, mid-, and late-type LFs are all consistent with the field LFs. However, the errors are such that one cannot yet argue convincingly for, or against, ubiquitous morphological LFs as proposed by BST88.

In exploring the luminosity- and number-density radial profiles, we find flat profiles for late types and argue that this implies an absence of late-type galaxies in the core region. Furthermore we find a significantly skewed luminosity-density breakdown toward early types, as compared with the field. We *speculate* that this implies that cluster cores are in essence disk-destroying engines resulting in the build up of a hot intercluster member and the formation of a tightly bound population of intermediate-luminosity core ellipticals most likely formed from mid-type bulges.

Finally from our error analysis we note that more definitive results can only be obtained from the combination of cluster data, since the dominant error at bright magnitudes is simply the number of cluster members. Such data is now becoming freely available via the Sloan Digital Sky Survey and the *HST* Archives. In this paper, we have laid down a rigorous methodology for the analysis of such data and look forward to an illuminating era.

We would like to thank Ray Lucas for help with the planning of the observations and Roberto De Propris and an anonymous referee for helpful comments on the manuscript. Support for program No. 8203 was provided by NASA through a grant from the Space Telescope Science Institute, which is operated by the Association of Universities for Research in Astronomy, Inc., under NASA contract NAS 5-26555.

REFERENCES

Baldry, I., et al. 2002, ApJ, 569, 582
Barkhouse, W. A., & Yee, H. C. 2002, in ASP Conf. Ser. 268, Tracing Cosmic Evolution with Galaxy Clusters, ed. S. Borgani, M. Mezzetti, & R. Valdarnini (San Francisco: ASP), 289
Bertin, E., & Arnouts, S. 1996, A&AS, 117, 393
Bingelli, B., Sandage, A., & Tammann, G. A. 1988, ARA&A, 26, 509 (BST88)
Bower, R. G., & Balogh, M. L. 2003, in Clusters of Galaxies: Probes of Cosmic Structure and Evolution, ed. J. S. Mulchaey, A. Dressler, & A. Oemler (Cambridge: Cambridge Univ. Press), in press
Boyce, P., Phillipps, S., Jones, J. B., Driver, S. P., Smith, R. M., & Couch, W. J. 2001, MNRAS, 328, 277
Christlein, D., & Zabludoff, A. 2003, ApJ, 591, 764
Cohen, S., Windhorst, R. A., Odewahn, S. C., Chiarenza, C. A., & Driver, S. P. 2003, AJ, 125, 1762
Cross, N. J. G., Driver, S. P., Liske, J., & Lemon, D. J. 2003, MNRAS, in press
De Propris, R., et al. 2003, MNRAS, 342, 725
de Vaucouleurs, G., de Vaucouleurs, A., Corwin, H. G., Buta, R. J., Paturel, G., & Fouqué, P. 1995, The Third Reference Catalogue of Galaxies (New York: Springer)
Dressler, A. 1980, ApJ, 236, 351
Dressler, A., et al. 1997, ApJ, 490, 577
Driver, S. P. 1999, ApJ, 526, L69
Driver, S. P., & De Propris, R. 2003, Ap&SS, 285, 175
Driver, S. P., Couch, W. J., & Phillipps, S. 1998a, MNRAS, 301, 369
Driver, S. P., Couch, W. J., Phillipps, S., & Smith, R. M. 1998b, MNRAS, 301, 357
Driver, S. P., Phillipps, S., Davies, J. I., Morgan, I., & Disney, M. J. 1994, MNRAS, 268, 393
Driver, S. P., Windhorst, R. A., Ostrander, E. J., Keel, W. M., Griffiths, R. E., & Ratnatunga, K. U. 1995, ApJ, 449, L23
Fruchter, A. S., & Hook, R. 2002, PASP, 114, 144
Fukugita, M., Ichikawa, T., Gunn, J. E., Doi, M., Shimasaku, K., & Schneider, D. P. 1996, AJ, 111, 1748
Gómez, P., et al. 2003, ApJ, 584, 210
Holtzmann, J. A., Burrows, C. J., Casertano, S., Hester, J. J., Trauger, J. T., Watson, A. M., & Worthey, G. 1995, PASP, 107, 1065
Lewis, I., et al. 2002, MNRAS, 334, 673
Liske, J., Lemon, D. J., Driver, S. P., Cross, N. J. G., & Couch, W. J. 2003, MNRAS, 344, 307
Lopez-Cruz, O. 1997, Ph.D. thesis, Univ. Toronto
Madgwick, D. S., et al. 2002, MNRAS, 333, 133
Marzke, R. O., da Costa, L. N., Pellegrini, P. S., Willmer, C. N. A., & Geller, M. J. 1998, ApJ, 503, 617
Moore, B., Lake, G., & Katz, N. 1998, ApJ, 499, L5
Nakamura, O., Fukugita, M., Yasuda, N., Loveday, J., Brinkmann, J., Schneider, D. P., Shimasaku, K., & SubbaRao, M. 2003, AJ, 125, 1682
Odewahn, S. C., Cohen, S., Windhorst, R. A., & Ninan Sajeeth, P. 2002, ApJ, 568, 539
Odewahn, S. C., Windhorst, R. A., Driver, S. P., & Keel, W. C. 1996, ApJ, 472, L13
Peebles, J. P. E. 1980, in The Large-Scale Structure of the Universe (Princeton: Princeton Univ. Press)
Phillipps, S., & Disney, M. J. 1985, A&A, 148, 234
Phillipps, S., Driver, S. P., Couch, W. J., & Smith, R. M. 1998, ApJ, 498, L119
Poggianti, B. 1997, A&AS, 122, 399
Pracy, M., de Propris, R., Couch, W. J., Bekki, K., Driver, S. P., & Nulsen, P. E. J. 2003, MNRAS, submitted
Roche, N., & Eales, S. 1999, MNRAS, 307, 703
Sabatini, S., Davies, J., Scaramella, R., Smith, R. M., Baes, M., Linder, S., Roberts, S., & Testa, V. 2003, MNRAS, 341, 981
Sandage, A., Bingelli, B., & Tammann, G. A. 1985, AJ, 90, 1759 (BST)
Schlegel, D., Finkbeiner, D. P., & Davis, M. 1998, ApJ, 500, 525
Smith, R. M., Driver, S. P., & Phillipps, S. 1997, MNRAS, 287, 415
Strubble, M. F., & Rood, H. J. 1999, ApJS, 125, 35
Sung, H., & Bessell, M. S. 2000, Publ. Astron. Soc. Australia, 17, 244
Thompson, L. A., & Gregory, S. A. 1993, AJ, 106, 2197
Trentham, N. 1998, MNRAS, 295, 360
Trentham, N., & Hodgkin, S. 2002, MNRAS, 333, 423
Trentham, N., & Tully, B. 2002, MNRAS, 335, 712
Valotto, C. A., Moore, B., & Lambas, D. G. 2001, ApJ, 546, 157
Windhorst, R. A., Keel, W. C., & Pascarelle, S. 1998, ApJ, 494, L27